Surface Reconstruction With Optimized Random Laser Plane Generated From Cylindrical Reference

GUAN XU[1], (Member, IEEE), JING YUAN[1], AND XIAOTAO LI[ID][2]

[1]Department of Vehicle Application Engineering, Transportation College, Jilin University, Changchun 130025, China
[2]School of Mechanical Science and Engineering, Jilin University, Nanling Campus, Changchun 130025, China

Corresponding author: Xiaotao Li (lixiaotao@jlu.edu.cn)

ABSTRACT A reconstruction approach is presented with a random laser plane and a cylindrical reference. A semi-cylinder reference with the known diameter is designed as the cylindrical-coordinate-system. The optimization function is provided by the parameterized re-projection errors of the feature points on the cylindrical reference, the laser intersection points on the cylindrical reference and the object. The reconstruction approach is tested and analyzed by contrasting the difference between the reconstructed value and the true value of the vernier caliper. The means of the root mean squares of the optimization and initialization are 1.36 and 1.44 mm, respectively. The experiments indicate that the approach with the random laser plane and the cylindrical reference is a reliable method for the 3-D reconstruction in the active vision system with the planar structured light.

INDEX TERMS Surface reconstruction, cylindrical reference, structured light.

I. INTRODUCTION

In recent years, vision-based measurement, as a branch of optical inspection, develops rapidly as it takes the advantages of the non-contact detection and the reasonable stability [1]–[4]. The vision measurement system captures an object image by the camera and transmits it to an image processing system for the surface information of the object [5], [6]. Therefore, the visual-based measurement system has the development potentials in the fields of industry, medicine, military and transportation, owing to the low cost, the high automation and the simple operation [7]–[9].

Two main vision measurement methods are reported in previous works to reconstruct the object surface: passive vision and active vision. In the vision measurement methods based on the passive vision, a camera is employed to capture the image and provide the 2D information in the image. However, a camera can only reconstruct the previsional 2D surface of an object, as the calibrated camera is a one-to-one mapping from the 2D information in the image to the 2D surface. Moreover, for a 3D object, it is impossible to reconstruct the surface by one camera without additional conditions. Therefore, the other camera is added in the measurement system, which is known as the stereo vision system. Two one-to-one mappings are contributed by the stereo vision system, which means four equations are prepared to solve a 3D point. Hence, the 3D point on the surface can be reconstructed by the stereo vision. Although the 3D points are acquired by the stereo vision technology, it is difficult to reconstruct the smooth 3D surface without the texture or corners. For this reason, a projector to generate the structured light is adopted to replace a camera in the stereo vision. The calibrated light is projected to the 3D object as the active mark. Thus the active vision system can reconstruct the 3D surface with or without the texture or corners.

A typical structured light measurement system consists of an object to be measured, a camera and a laser projector [10], [11]. The structured light measurement has been studied in recent years. Kiddee *et al.* [12] proposes a structured light system to track the weld seam. The crossing structured light is recognized in the region of interest (ROI) and considered as the input signal of the visual servo-loop system. Ha and Her [13] presents a method to convert the 3D measurement information from the camera-coordinate-system to the laser-projector-coordinate-system.

In the method, two perpendicular planar references are designed for the calibration. Then, the parameters of the camera and the pose of the laser projector are calibrated by the planar references. Xu *et al.* [14] introduces a method to calibrate the laser plane by a 1D reference with a mark on its top. The intersection point of the three planes of the 3D reference is defined as the origin of the world-coordinate-system. The bottom tip of the 1D reference coincides with the world coordinate origin. The coordinates of the laser plane are optimized by minimizing the difference between the parameterized distance and the length of the 1D reference. In the structured-light-based vision measurement system, the accuracy of the camera calibration has direct impact on the measurement results. Therefore, it is important to choose the appropriate method to calibrate the camera. At present, three main calibration methods include the 3D reference on the basis of a cube [15], [16], the 2D reference on the basis of a plane [17]–[19] and the 1D reference on the basis of a bar [20], [21]. The 1D reference is easy to be manufactured. However, the 1D reference method requires at least six photographs of the target to calibrate the camera. Moreover, the calibration accuracy of the 1D reference method is lower than those of the 2D and 3D reference methods for the linear correlation of the coordinates on the 1D reference. Consequently, the 2D or 3D reference methods are more reasonable for the measurement. The 2D reference method accomplishes the calibration by obtaining at least three reference images. It also needs to change the pose of the reference during the calibration process although the 2D reference is easy to be made and moved. The 3D reference method on the basis of a cube only requires a reference image to calibrate the camera. The target position is not changed in the experiment. Moreover, the 3D reference method has higher accuracy and better stability. A precise camera calibration plays an important role in the 3D reconstruction, which refers to the process of obtaining the 3D information from single or multi-view images [22]. Moeini and Moeini [23] outlines a novel method to classify the gender by the reconstructed 3D face model from the front-view images. The feature library matrix is derived from the rotations of the 3D model. Then, an array of the feature library matrix is selected on the basis of the yaw angle estimation. Finally, the selected array is compared with the features of the target image. A novel linear framework is illustrated by Koo and Kim [24] to achieve the 3D reconstruction and the camera calibration by applying the scene geometry in the images. The method adopts the constraints of parallelism, coplanarity, colinearity and orthogonality of the object. Therefore, results are obtained only by the linear operations. The cubic reference is chosen as the auxiliary instrument to determine the position of the laser plane in the measurement [25], where the laser plane is flexible. However, for the large object, it is difficult to manufacture the cube that covers the object. Therefore, the bi-cuboid references are designed to simulate an extendible reference and the camera parameters are provided by the balance model [26]. Moreover, the laser plane is calculated by the bi-planar

references as the references are easier to be manufactured [27]. Although the cubic reference is more accurate than the planar reference, the projection points of the cubic reference are not even-distributed in the image, which reduces the measurement accuracy. The bi-cuboid references and the bi-planar references also take the above problem. Hence, a cylindrical reference is chosen as the auxiliary instrument to position the laser plane and provide the even projections of the feature points.

A recovery approach of the 3D object is achieved by a random laser plane and the cylindrical reference in this paper. A semi-cylinder with the known diameter is employed as the 3D reference. Although the surface reconstruction can be achieved by the traditional cubic reference, the reconstruction accuracy problem influences the applications of the method with the cubic reference. The cubic reference is made by two or three boards, which are perpendicular to each other. As the projections of the feature points on the boards of the cubic reference are not even-distributed in the image, the reconstruction accuracy employing the cubic reference is impacted by the un-even projections of the feature points. However, the cylindrical reference is a quasi-isotropic reference, which provides the even-distributed points in the image. The feature points on the cylindrical reference distribute uniformly than the ones on the cube reference in the image. The transformation matrix between the world-coordinate-system and the image- coordinate-system is obtained by the projection of the cylindrical reference. The laser plane is generated from the projections of the intersection points on the cylindrical reference. The initial solutions of the points on the object are derived from the laser plane. The optimization function is created to improve the reconstruction precision by minimizing the parameterized re-projection errors. The accuracy of the approach is evaluated by comparing the differences between the reconstructed value and the true value of the vernier caliper.

II. RECONSTRUCTION APPROACH

The reconstruction method of a random laser plane with a cylindrical reference is illustrated in Fig. 1. The measurement system consists of a cylindrical reference with checkerboard pattern, a random laser plane and a camera. The cylindrical coordinate system, which is attached on the cylindrical reference, is considered as the world-coordinate-system. The image-coordinate-system is defined on the image. C is the optical center. The reconstruction process of the initial solution is interpreted in Fig. 2.

From the pinhole model [28], the projection from the feature point on the cylindrical reference to the image point is given by

$$\mathrm{P}\mathbf{M}_i^{(C)} = s_i^{(C)}\mathbf{m}_i^{(C)} \tag{1}$$

where $\mathrm{P} = [p_{mn}]_{3\times4}$ is the projection matrix, $\mathbf{M}_i^{(C)} = (r\cos\theta, r\sin\theta, Z_i^{(C)}, 1)^{\mathrm{T}}$ is the 3D cylindrical coordinate, r is the radius of the cylinder reference, θ is the polar angle
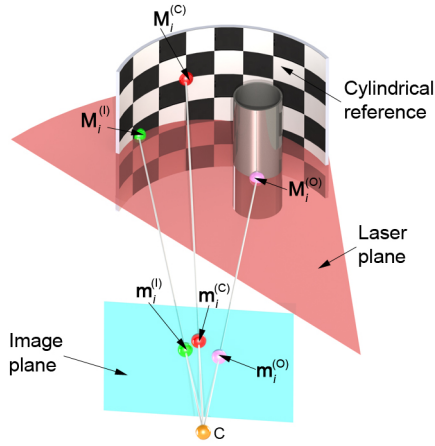
FIGURE 1. The reconstruction approach using a laser plane, a cylindrical reference and a camera.
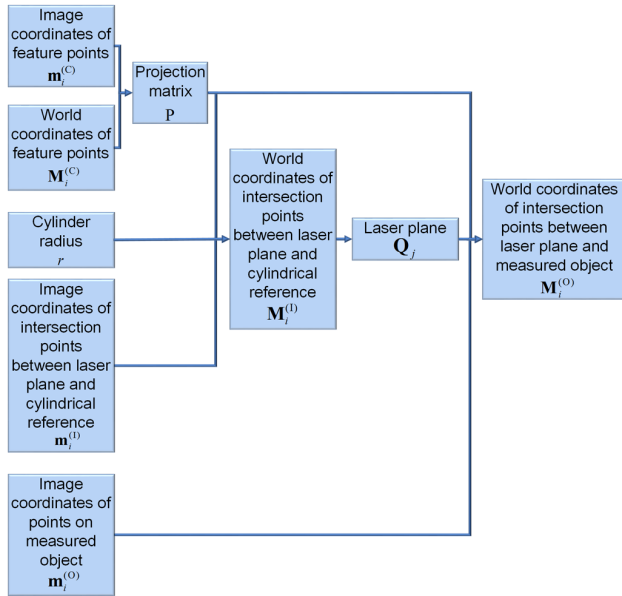

FIGURE 2. The 3D reconstruction process of the initial solution adopting the random laser plane and the cylindrical reference.

of $\mathbf{M}_i^{(C)}$, $\mathbf{m}_i^{(C)} = (x_i^{(C)}, y_i^{(C)}, 1)^{\mathrm{T}}$ is the 2D projective point of $\mathbf{M}_i^{(C)}$, $s_i^{(C)}$ is the scale factor. The projection matrix P can be determined by the direct linear transform [16].

Based on the pinhole model [28], for the intersection points on the cylindrical reference, the projection is expressed by

$$\mathrm{P}\mathbf{M}_i^{(I)} = s_i^{(I)}\mathbf{m}_i^{(I)} \tag{2}$$

where $\mathbf{M}_i^{(I)} = (X_i^{(I)}, Y_i^{(I)}, Z_i^{(I)}, 1)^{\mathrm{T}}$ is the 3D coordinate of the intersection point, $\mathbf{m}_i^{(I)} = (x_i^{(I)}, y_i^{(I)}, 1)^{\mathrm{T}}$ is the 2D projection of $\mathbf{M}_i^{(I)}$, $s_i^{(I)}$ is the scale factor.

According to Eq. (2), then

$$\begin{aligned} X_i^{(I)} &= a_{1i}Z_i^{(I)} + b_{1i} \\ Y_i^{(I)} &= a_{2i}Z_i^{(I)} + b_{2i} \end{aligned} \tag{3}$$

where a_{1i}, b_{1i}, a_{2i}, and b_{2i}, as shown at the bottom of the next page.

The intersection point $\mathbf{M}_i^{(I)}$ is located on the cylindrical reference. Then, it satisfies

$$\begin{cases} (X_i^{(I)})^2 + (Y_i^{(I)})^2 = r^2 \\ Z_i^{(I)} = Z_i^{(I)} \end{cases} \tag{4}$$

Stacking Eqs. (3) and (4), then

$$a_i(Z_i^{(I)})^2 + b_iZ_i^{(I)} + c_i = 0 \tag{5}$$

where $a_i = a_{1i}^2 + a_{2i}^2$, $b_i = 2(a_{1i}b_{1i} + a_{2i}b_{2i})$, $c_i = b_{1i}^2 + b_{2i}^2 - r^2$, $Z_i^{(I)} = \left(-b_i \pm \sqrt{b_i^2 - 4a_ic_i}\right)/2a_i$. As $Z_i^{(I)}$ in the cylindrical coordinate system is larger than zero, we can determine the sign in $Z_i^{(I)}$. Furthermore, $\mathbf{M}_i^{(I)}$ is solved by Eqs. (3) and (5).

As the intersection point $\mathbf{M}_i^{(I)}$ is positioned on the laser plane $\mathbf{Q}_j$, then [28]

$$(\mathbf{M}_i^{(I)})^{\mathrm{T}}\mathbf{Q}_j = 0 \tag{6}$$

where the laser plane $Q_j = (Q_{1j}, Q_{2j}, Q_{3j}, 1)^{\mathrm{T}}$ [29].

The object point $\mathbf{M}_i^{(O)} = (X_i^{(O)}, Y_i^{(O)}, Z_i^{(O)}, 1)^{\mathrm{T}}$ is also located on $\mathbf{Q}_j$, then [28]

$$(\mathbf{Q}_j)^{\mathrm{T}}\mathbf{M}_i^{(O)} = 0 \tag{7}$$

The point $\mathbf{M}_i^{(O)}$ on the measured object is projected by the pinhole model [28] to the image point $\mathbf{m}_i^{(O)} = (x_i^{(O)}, y_i^{(O)}, 1)^{\mathrm{T}}$ and satisfies

$$\mathrm{P}\mathbf{M}_i^{(O)} = s_i^{(O)}\mathbf{m}_i^{(O)} \tag{8}$$

where $s_i^{(O)}$ is the scale factor.

From Eqs. (7) and (8), the reconstructed coordinate of the point $\mathbf{M}_i^{(O)}$ on the measured object is

$$\begin{aligned} X_i^{(O)} = & \{Q_{2j}[(p_{34}y - p_{24})(p_{33}x - p_{13}) - (p_{34}x - p_{14}) \\ & \times (p_{33}y - p_{23})][(p_{31}x - p_{11})(p_{33}y - p_{23}) \\ & - (p_{31}y - p_{21})(p_{33}x - p_{13})] + Q_{3j}[(p_{32}y - p_{22}) \\ & \times (p_{33}x - p_{13}) - (p_{32}x - p_{12}) \\ & \times (p_{33}y - p_{23})][(p_{31}x - p_{11})(p_{34}y - p_{24}) \\ & - (p_{31}y - p_{21})(p_{34}x - p_{14})] + Q_{3j}[(p_{34}y - p_{24}) \\ & \times (p_{33}x - p_{13}) - (p_{34}x - p_{14})(p_{33}y - p_{23})] \\ & \times [(p_{32}x - p_{12})(p_{31}y - p_{21}) - (p_{31}x - p_{11}) \\ & \times (p_{32}y - p_{22})]\}\{ Q_{1j}[(p_{32}y - p_{22})(p_{33}x - p_{13}) \\ & - (p_{32}x - p_{12})(p_{33}y - p_{23})] + Q_{2j}[(p_{31}x - p_{11}) \\ & \times (p_{33}y - p_{23}) - (p_{31}y - p_{21})(p_{33}x - p_{13})] \\ & + Q_{3j}[(p_{32}x - p_{12})(p_{31}y - p_{21}) - (p_{31}x - p_{11}) \\ & \times (p_{32}y - p_{22})]\}^{-1}[(p_{31}x - p_{11})(p_{33}y - p_{23}) \\ & - (p_{31}y - p_{21})(p_{33}x - p_{13})]^{-1} \\ Y_i^{(O)} = & \{Q_{1j}[(p_{34}x - p_{14})(p_{33}y - p_{23}) - (p_{34}y - p_{24}) \\ & \times (p_{33}x - p_{13})] + Q_{3j}[(p_{31}x - p_{11})(p_{34}y - p_{24}) \\ & - (p_{31}y - p_{21})(p_{34}x - p_{14})]\}\{Q_{1j}[(p_{32}y - p_{22}) \end{aligned}$$

$$
\times (p_{33}x - p_{13}) - (p_{32}x - p_{12})(p_{33}y - p_{23})]
$$
$$
+ Q_{2j}[(p_{31}x - p_{11})(p_{33}y - p_{23}) - (p_{31}y - p_{21})
$$
$$
\times (p_{33}x - p_{13})] + Q_{3j}[(p_{32}x - p_{12})(p_{31}y - p_{21})
$$
$$
- (p_{31}x - p_{11})(p_{32}y - p_{22})]\}^{-1}
$$
$$
Z_i^{(O)} = \{ Q_{1j}[(p_{31}x - p_{11})(p_{32}y - p_{22}) - (p_{32}x - p_{12})
$$
$$
\times (p_{31}y - p_{21})][(p_{34}x - p_{14})(p_{33}y - p_{23})
$$
$$
- (p_{34}y - p_{24})(p_{33}x - p_{13})] + Q_{1j}[(p_{31}x - p_{11})
$$
$$
\times (p_{34}y - p_{24}) - (p_{31}y - p_{21})(p_{34}x - p_{14})]
$$
$$
\times [(p_{32}y - p_{22})(p_{33}x - p_{13}) - (p_{32}x - p_{12})
$$
$$
\times (p_{33}y - p_{23})] + Q_{2j}[(p_{31}x - p_{11})(p_{34}y - p_{24})
$$
$$
- (p_{31}y - p_{21})(p_{34}x - p_{14})][(p_{31}x - p_{11})
$$
$$
\times (p_{33}y - p_{23}) - (p_{31}y - p_{21})(p_{33}x - p_{13})]\}
$$
$$
\times \{ Q_{1j}[(p_{32}y - p_{22})(p_{33}x - p_{13}) - (p_{32}x - p_{12})
$$
$$
\times (p_{33}y - p_{23})] + Q_{2j}[(p_{31}x - p_{11})(p_{33}y - p_{23})
$$
$$
- (p_{31}y - p_{21})(p_{33}x - p_{13})] + Q_{3j}[(p_{32}x - p_{12})
$$
$$
\times (p_{31}y - p_{21}) - (p_{31}x - p_{11})(p_{32}y - p_{22})]\}^{-1}
$$
$$
\times [(p_{31}y - p_{21})(p_{33}x - p_{13})
$$
$$
- (p_{31}x - p_{11})(p_{33}y - p_{23})]^{-1} \tag{9}
$$

The initial value of $\mathbf{M}_i^{(O)}$ is solved by Eq. (9). However, the initial solution should be refined by optimization method as the noise impacts the reconstruction accuracy. The optimization process of the 3D reconstruction with the random laser plane and the cylindrical reference is explained by the flow diagram in Fig. 3.

Here, we consider three main factors to generate the optimization objective function. First, the re-projection image point of the feature point $\mathbf{M}_i^{(C)}$ on the cylindrical reference should approach the real feature point $\mathbf{m}_i^{(C)}$ in the image. In a similar way, the re-projection image points of the points $\mathbf{M}_i^{(I)}$ and $\mathbf{M}_i^{(O)}$ should also approach to the corresponding points $\mathbf{m}_i^{(I)}$ and $\mathbf{m}_i^{(O)}$ in the image. The different between them are

$$
f(\mathrm{P}, \mathbf{Q}_j) = \sum_{i=1}^{n} \left\{ \left\| \mathrm{P}\mathbf{M}_i^{(C)} - s_i^{(C)}\mathbf{m}_i^{(C)} \right\|^2 \right.
$$
$$
\left. + \left\| \mathrm{P}\mathbf{M}_i^{(I)} - s_i^{(I)}\mathbf{m}_i^{(I)} \right\|^2 + \left\| \mathrm{P}\mathbf{M}_i^{(O)} - s_i^{(O)}\mathbf{m}_i^{(O)} \right\|^2 \right\} \tag{10}
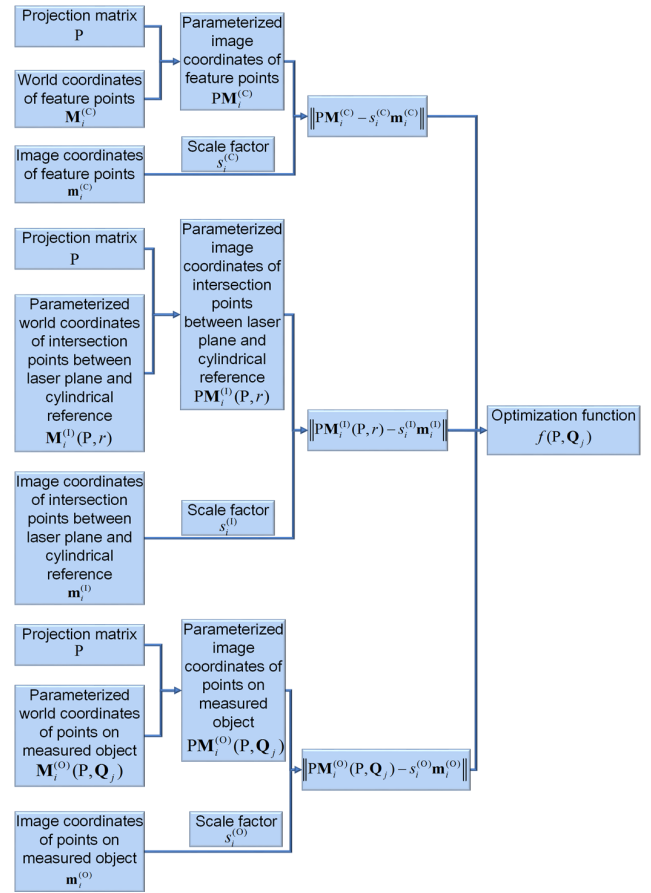$$

FIGURE 3. The 3D reconstruction diagram of the optimization adopting the random laser plane and the cylindrical reference.

From the condition in Eq. (10), the parameterized integrative optimization function to be minimized is

$$
f(\mathrm{P}, \mathbf{Q}_j) = \sum_{i=1}^{n} \left\{ \left\| \mathrm{P}\mathbf{M}_i^{(C)} - s_i^{(C)}\mathbf{m}_i^{(C)} \right\|^2 \right.
$$
$$
+ \left\| \mathrm{P}\mathbf{M}_i^{(I)}(P, r) - s_i^{(I)}\mathbf{m}_i^{(I)} \right\|^2
$$
$$
\left. + \left\| \mathrm{P}\mathbf{M}_i^{(O)}(P, \mathbf{Q}_j) - s_i^{(O)}\mathbf{m}_i^{(O)} \right\|^2 \right\} \tag{11}
$$

$$
a_{1i} = \frac{[(p_{33}y_i^{(I)} - p_{23})(p_{32}x_i^{(I)} - p_{12}) - (p_{33}x_i^{(I)} - p_{13})(p_{32}y_i^{(I)} - p_{22})]}{(p_{31}x_i^{(I)} - p_{11})(p_{32}y_i^{(I)} - p_{22}) - (p_{31}y_i^{(I)} - p_{21})(p_{32}x_i^{(I)} - p_{12})}
$$
$$
b_{1i} = \frac{(p_{34}y_i^{(I)} - p_{24})(p_{32}x_i^{(I)} - p_{12}) - (p_{34}x_i^{(I)} - p_{14})(p_{32}y_i^{(I)} - p_{22})}{(p_{31}x_i^{(I)} - p_{11})(p_{32}y_i^{(I)} - p_{22}) - (p_{31}y_i^{(I)} - p_{21})(p_{32}x_i^{(I)} - p_{12})}
$$
$$
a_{2i} = \frac{[(p_{33}y_i^{(I)} - p_{23})(p_{31}x_i^{(I)} - p_{11}) - (p_{33}x_i^{(I)} - p_{13})(p_{31}y_i^{(I)} - p_{21})]}{(p_{32}x_i^{(I)} - p_{12})(p_{31}y_i^{(I)} - p_{21}) - (p_{32}y_i^{(I)} - p_{22})(p_{31}x_i^{(I)} - p_{11})}
$$
$$
b_{2i} = \frac{(p_{34}y_i^{(I)} - p_{24})(p_{31}x_i^{(I)} - p_{11}) - (p_{34}x_i^{(I)} - p_{14})(p_{31}y_i^{(I)} - p_{21})}{(p_{32}x_i^{(I)} - p_{12})(p_{31}y_i^{(I)} - p_{21}) - (p_{32}y_i^{(I)} - p_{22})(p_{31}x_i^{(I)} - p_{11})}.
$$

where P, $\mathbf{Q}_j$ are the optimized parameters and generated from the minimum of Eq. (11). According to the optimized P, $\mathbf{Q}_j$ from Eq. (11), the optimized point $\mathbf{M}_i^{(O)}$ is reconstructed by Eq. (9).

III. EXPERIMENTS AND DISCUSSIONS

A half cylinder with the diameter of 305 mm is selected as the cylindrical reference in the experiments. The distance between adjacent corner points along the surface of the cylindrical reference is 30 mm. The height of the cylindrical reference is 400 mm. The images with the resolution of 2048 × 1536 are captured by the industrial camera in the experiments. In order to obtain the enough information of the cylindrical reference, 42 points are uniformly selected on the cylindrical reference. In the process of the camera calibration, Harris corner recognition [30] is used to recognize the points on the cylindrical reference in the image.

The reconstruction results with the random laser plane and cylindrical reference are showed in Fig. 4. Figures 4(a), 4(c), 4(e) and 4(g) represent four experiments in which the measured objects are the cylindrical tube, the flat surface, the pencil vase and the hot water bottle. The reconstruction results of experiments are presented in Figs. 4(b), 4(d), 4(f) and 4(h) where the laser plane is located at 10 different positions. The points of the intersection curve can be modeled by Eq. (9). The red balls represent the selected feature points of the cylindrical reference. The green balls show the intersection points between the laser plane and the cylindrical reference. In the four groups of experiments, 40 points on the intersection curve are selected to solve the equation of the laser plane. The blue balls indicate 20 points of the intersection curve between the laser plane and the object being measured.

A vernier caliper with known measurements is employed as the test benchmark to verify the accuracy of the method. Two semicircle markers are pasted on the outside large jaws of the vernier caliper. The distances between the two marker centers on the vernier caliper are from 20 mm to 80 mm with the interval of 20 mm. In Fig. 5, the vernier caliper is located in the view field. The laser plane is projected on the vernier caliper. Two intersection points $\mathbf{M}_k^{(O)}$ and $\mathbf{M}_{k+1}^{(O)}$ are chosen as the test points, which are reconstructed by the optimization function Eqs. (11) and (9). The reconstruction error is defined by

$$\Delta_k = \left\| \mathbf{M}_k^{(O)} - \mathbf{M}_{k+1}^{(O)} \right\| - L_0 \qquad (12)$$

where L_0 is the benchmark distance between the two marker centers on the vernier caliper.

A vernier caliper with the known measurement is adopted as the benchmark distance. The distances between the two marker centers on the vernier caliper are from 20 mm to 80 mm with the interval of 20 mm. The camera-object distances are from 600 mm to 1200 mm with the interval of 200 mm. The reconstruction errors of the initial method and the optimization method are shown in Fig. 6.
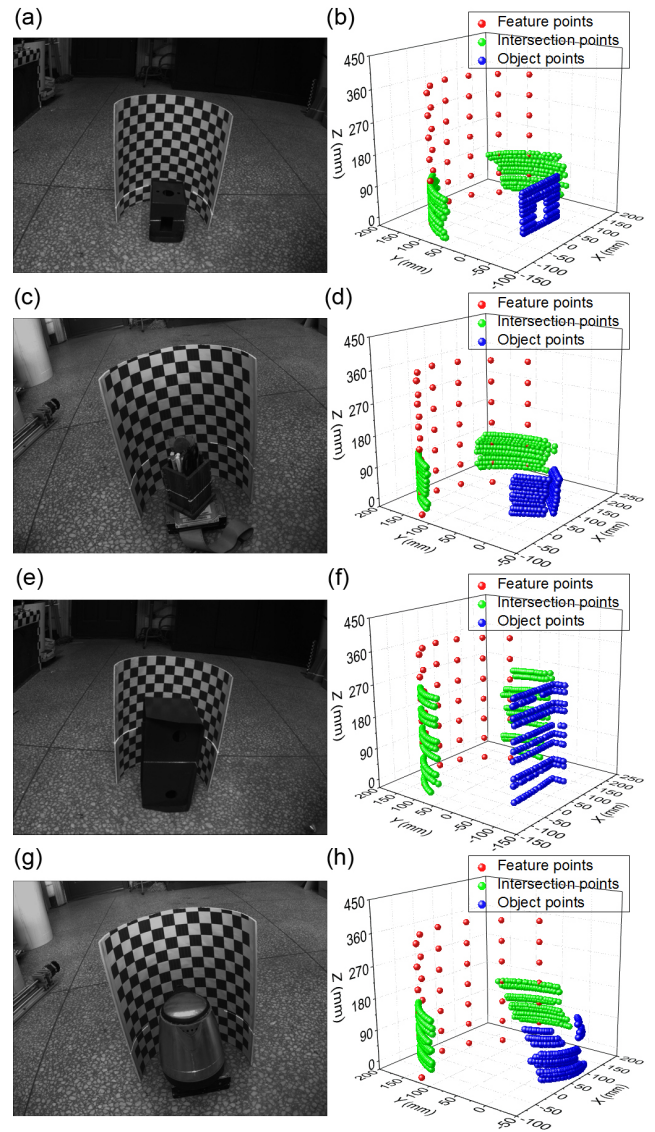

FIGURE 4. The reconstruction experiments with the random laser plane and cylindrical reference. (a) The experiment of a cubic with holes. (b) The recovery results of the cubic with holes. (c) The experiment of the pencil vase. (d) The recovery results of the pencil vase. (e) The experiment of a mechanical part. (f) The recovery results of the mechanical part. (g) The experiment of the hot water bottle. (h) The recovery results of the hot water bottle.

The statistical data are listed in Table 1 and Table 2. The error ranges of the optimization are 0.07 mm-0.98 mm, 0.26 mm-1.46 mm, 0.74 mm-2.01 mm and 1.65 mm-2.86 mm, for the benchmark distances from 20 mm to 80 mm. The corresponding error ranges of the initialization are 0.09 mm-0.99 mm, 0.30 mm-2.10 mm and 1.73 mm-2.97 mm, respectively. The error ranges of the optimization are 0.33 mm-2.79 mm, 0.11 mm-2.80 mm, 0.07 mm-2.82 mm and 0.14 mm-2.86 mm, for the camera-object distances from 600 mm to 1200 mm. The related error ranges of initialization are 0.34 mm-2.91 mm, 0.13 mm-2.97 mm, 0.09 mm-2.88 mm and 0.24 mm-2.94 mm, respectively. The relative errors of the optimization under the 600 mm distance between the camera
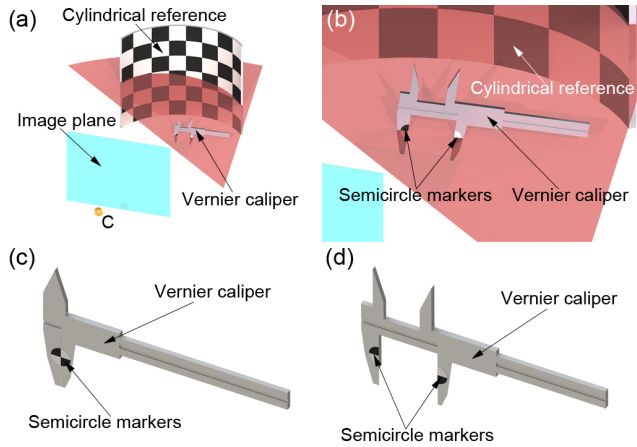
FIGURE 5. The verification method adopting a vernier caliper with two semicircle markers. The benchmark distances in the verifications are from 20 mm to 80 mm with the interval of 20 mm. (a) The point reconstructions of the two markers on the vernier caliper in the verification. (b) Enlarged details of the verification instruments. (c) Two semicircle marker on the outside large jaws of the vernier caliper. (d) The vernier caliper provides an accurate distance as the benchmark.

and the cylindrical reference are 2.66%, 2.49%, 2.44% and 3.02%, with the distances between the two marker centers from 20 mm to 80 mm. The related relative errors of the initialization are respectively 2.86%, 2.67%, 2.66% and 3.25%. The relative errors of the optimization under the 800 mm distance between the camera and the cylindrical reference are 2.48%, 2.31%, 2.35% and 3.00%, with the distances between the two marker centers from 20 mm to 80 mm. The related relative errors of the initialization are 2.63%, 2.54%, 2.54% and 3.23%, respectively. The relative reconstruction errors of the optimization under the 1000 mm distance between the camera and the cylindrical reference are 2.39%, 2.19%, 2.28% and 2.93%, with the distances between the two marker centers from 20 mm to 80 mm. The relative reconstruction errors of the initialization are 2.47%, 2.28%, 2.37% and 3.02%, respectively. The relative reconstruction errors of the optimization under the 1200 mm distance between the camera and the cylindrical reference are 2.50%, 2.51%, 2.40% and 3.25%, with the distances between the two marker centers from 20 mm to 80 mm. The relative reconstruction errors of the initialization are 2.85%, 2.68%, 2.65% and 3.37%, respectively.

According to the experiment results above, the relative errors are smaller than 5%. The means and root mean squares (RMS) show the increasing trend with the increasing distance between the two marker centers. The means and RMS of the optimization are smaller than those of the initialization in the four groups of experiments with the different distances between the camera and the cylindrical reference. It shows that the optimization method provides the good precision and stability in the experiments. Moreover, the average values and RMS of the reconstruction errors under the 1000 mm distance between the camera and the cylindrical reference are
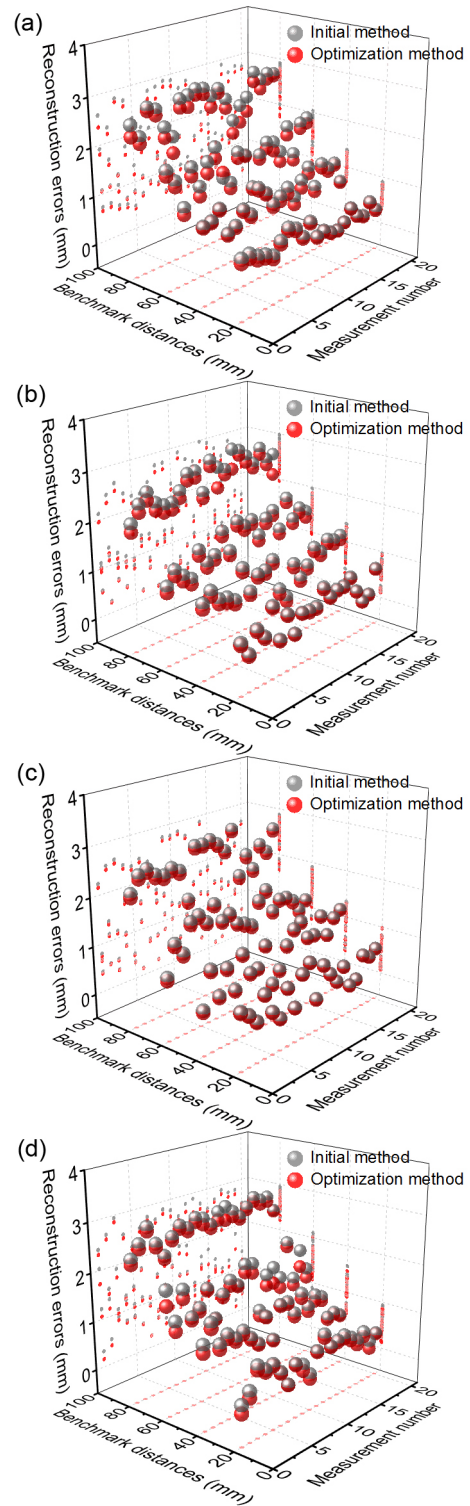

FIGURE 6. The reconstruction errors of the initial method and the optimization method. The benchmark distances are from 20 mm to 80 mm with the interval of 20 mm. The distances of (a)-(d), between the camera and the cylindrical reference, are from 600 mm to 1200 mm with the interval of 200 mm.

the smallest in the experiments. In addition, the averages and RMS of the reconstruction errors under the 800 mm distance between the camera and the cylindrical reference are less than

TABLE 1. The statistic values of the reconstruction errors.

No.	Method		Benchmark distance, mm			
			20	40	60	80
1	Initial method, mm	Min.	0.34	0.73	0.91	2.00
		Max.	0.89	1.37	2.03	2.91
		Mean	0.57	1.07	1.59	2.60
		RMS	0.60	1.09	1.62	2.62
	Optimization method, mm	Min.	0.33	0.70	0.86	1.73
		Max.	0.84	1.33	1.82	2.79
		Mean	0.53	1.00	1.46	2.41
		RMS	0.55	1.02	1.49	2.44
2	Initial method, mm	Min.	0.13	0.40	1.07	2.12
		Max.	0.96	1.39	1.97	2.97
		Mean	0.53	1.01	1.52	2.58
		RMS	0.57	1.04	1.54	2.59
	Optimization method, mm	Min.	0.11	0.30	0.96	1.96
		Max.	0.93	1.32	1.87	2.80
		Mean	0.50	0.93	1.41	2.40
		RMS	0.54	0.96	1.44	2.41
3	Initial method, mm	Min.	0.09	0.30	0.80	1.73
		Max.	0.99	1.33	1.90	2.88
		Mean	0.49	0.91	1.42	2.41
		RMS	0.55	0.96	1.45	2.43
	Optimization method, mm	Min.	0.07	0.26	0.74	1.65
		Max.	0.98	1.30	1.85	2.82
		Mean	0.48	0.88	1.37	2.35
		RMS	0.54	0.93	1.40	2.37
4	Initial method, mm	Min.	0.24	0.57	0.88	2.27
		Max.	0.93	1.57	2.10	2.94
		Mean	0.57	1.07	1.59	2.69
		RMS	0.60	1.11	1.62	2.70
	Optimization method, mm	Min.	0.14	0.54	0.76	2.21
		Max.	0.85	1.46	2.01	2.86
		Mean	0.50	1.01	1.44	2.60
		RMS	0.55	1.04	1.47	2.60

TABLE 2. The statistic values of the relative reconstruction errors.

No.	Method	Benchmark distance, mm			
		20	40	60	80
1	Initial method, %	2.86	2.67	2.66	3.25
	Optimization method, %	2.66	2.49	2.44	3.02
2	Initial method, %	2.63	2.54	2.54	3.23
	Optimization method, %	2.48	2.31	2.35	3.00
3	Initial method, %	2.47	2.28	2.37	3.02
	Optimization method, %	2.39	2.19	2.28	2.93
4	Initial method, %	2.85	2.68	2.65	3.37
	Optimization method, %	2.50	2.51	2.40	3.25

those under the 600 mm distance. While the averages and RMS of the reconstruction errors under the 1200 mm distance are the largest in the experiments.

The comparison experiments between the cylindrical reference and cubic reference are shown in Fig. 7. The mean error of the cylindrical-reference experiments is 0.84 mm, whereas the mean error of the cubic-reference experiments is 0.92 mm. In most cases, the smaller reconstruction errors are contributed by the cylindrical reference.

The comparison experiments are analyzed by the projection process. The projection process is further modeled to demonstrate the difference between the cubic reference and the cylindrical reference for the reconstruction.
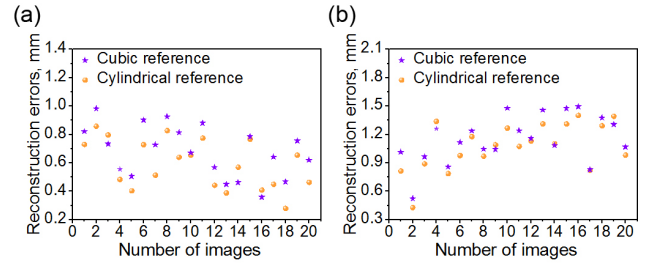

FIGURE 7. The experimental errors of the cubic-reference and the cylindrical-reference methods. (a) The benchmark distance is 20 mm. (b) The benchmark distance is 40 mm.
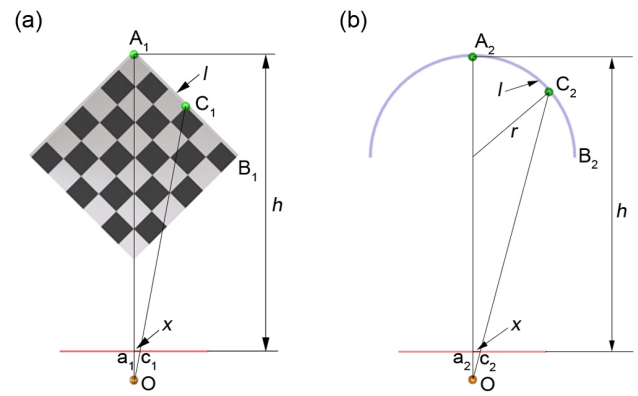

FIGURE 8. The principle analyses of the cubic reference and the cylindrical reference. (a) The mapping geometry of the cubic reference. (b) The mapping geometry of the cylindrical reference.

The projection model is illustrated in Fig. 8. O is the optical center of the camera. The points on the cubic reference and cylindrical reference are projected on the image planes. A typical 3D point C_1 on the interval of $[A_1, B_1]$ is chosen on the cubic reference. A typical 3D point C_2 on the interval of $[A_2, B_2]$ is chosen on the cylindrical reference. Here, as the z-coordinate is the same for the two 3D points, we consider the points C_1 and C_2 in the horizontal plane. The 3D points A_1, A_2 move to C_1, C_2 along the A_1B_1 and A_2B_2 directions, respectively. a_1, $\mathbf{a}_2$, c_1, c_2 are the image projections of A_1, A_2, C_1, C_2, respectively. For a fair evaluation, the movement distances A_1C_1, A_2C_2 are of the same value l. The distances from the image planes to the tops of the references are of the same value h. f is the focal length of the camera. Therefore, the distance between the projection point c_1 and the projection point a_1 is

$$x_1 = \frac{\sqrt{2}lf}{2h + 2f - \sqrt{2}l} \qquad (13)$$

The derivative of the projection distance x_1 is

$$\frac{dx_1}{dl} = \frac{2\sqrt{2}(h+f)f}{(2h + 2f - \sqrt{2}l)^2} \qquad (14)$$
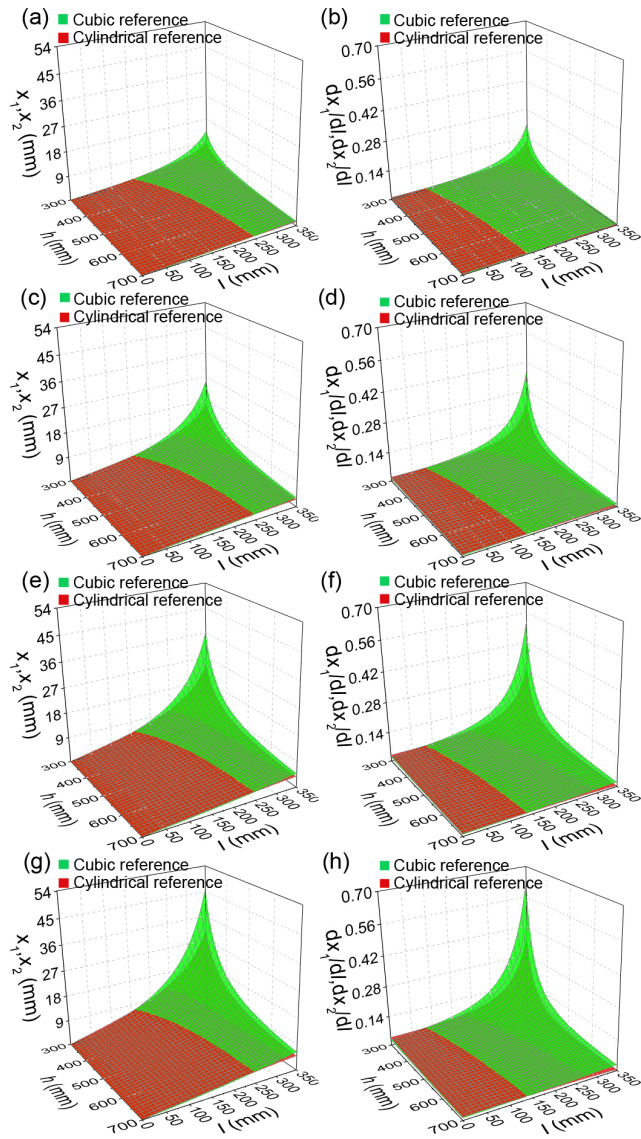
FIGURE 9. The projection distances x_1, x_2 and the derivatives dx_1/l, dx_2/l of the cubic reference and the cylindrical reference. (a) The projection distances x_1, x_2, $f = 3$ mm. (b) The derivatives dx_1/l, dx_2/l, $f = 3$ mm. (c) The projection distances x_1, x_2, $f = 6$ mm. (d) The derivatives dx_1/l, dx_2/l, $f = 6$ mm. (e) The projection distances x_1, x_2, $f = 9$ mm. (f) The derivatives dx_1/l, dx_2/l, $f = 9$ mm. (g) The projection distances x_1, x_2, $f = 12$ mm. (h) The derivatives dx_1/l, dx_2/l, $f = 12$ mm.

For the cylindrical reference, the distance between the projection point c_2 and the projection point a_2 is

$$x_2 = \frac{rf \sin(l/r)}{h + f - r + r\cos(l/r)} \qquad (15)$$

The derivative of the projection distance x_2 is

$$\frac{dx_2}{dl} = \frac{f\cos(l/r)(h+f-r+r\cos(l/r)) + rf\sin^2(l/r)}{(h+f-r+r\cos(l/r))^2} \qquad (16)$$

where r is the radius of the cylindrical reference.

From Eqs. (13)-(16), the image distances x_1 x_2 and the derivatives dx_1/l, dx_2/l are demonstrated in Fig. 9. When the

distances h and l are constants, with the increase of the focal length f, the image distances and the derivatives to the distance l both increases. The image distances and the derivatives of cylindrical reference are slightly higher than those of the cubic reference in the beginning. And then the image distances and the derivatives of cylindrical reference are less than those of the cubic reference with the increase of the distance l. In other words, the image distance of the cylindrical reference varies more smoothly than the one of the cubic reference. Hence, the cylindrical reference approaches to the isotropic reference in the reconstruction. As the feature points on the cylindrical reference are evenly projected to the image, the reconstruction accuracy is improved in the experiments.

IV. CONCLUSION
A reconstruction approach based on the random laser plane and the cylindrical reference is indicated in this paper. A semi-cylinder with the known diameter is adopted to obtain the transformation between the world-coordinate-system and the image-coordinate-system. The intersection points between the laser plane and the cylindrical reference are extracted to establish the equation of the laser plane. The optimization function is proposed by minimizing the parameterized re-projection errors. The reconstruction approach is verified by contrasting the difference between the reconstructed distance and the true distance. The means of the absolute errors and the relative errors are 1.33 mm and 2.58% in the optimization method. However, the corresponding means of the absolute and the relative errors are 1.42 mm and 2.75% in the initial method. Furthermore, the proposed method contributes the relative errors that are smaller than 5%. The means and RMS present the increasing trend with the rising distance between the two marker centers. The average values and RMS of the reconstruction errors is the smallest ones under the 1000 mm distance between the camera and the cylindrical reference. The results of the experiment confirm that the reconstruction approach with the random laser plane and cylindrical reference takes a high accuracy and stability. The surface reconstruction method has the application potentials in many measurement fields, e.g. mechanical production, skeleton remanufacture and reverse engineering, due to the low cost, the high automation and the simple operation. This method is of great significance for the size measurement of mechanical parts and other applications of 3D reconstruction.

REFERENCES
[1] N. Farid, H. Hussein, and M. Bahrawi, "Employing of diode lasers in speckle photography and application of FFT in measurements," *MAPAN*, vol. 30, no. 2, pp. 125–129, 2015.
[2] A. Głowacz and Z. Głowacz, "Diagnosis of the three-phase induction motor using thermal imaging," *Infr. Phys. Technol.*, vol. 81, pp. 7–16, Mar. 2017.
[3] Y. Cai, Z. Liu, H. Wang, and X. Sun, "Saliency-based pedestrian detection in far infrared images," *IEEE Access*, vol. 5, pp. 5013–5019, 2017.
[4] I. Frollo, A. Krafčík, P. Andris, J. Přibil, and T. Dermek, "Circular samples as objects for magnetic resonance imaging—Mathematical simulation, experimental results," *Meas. Sci. Rev.*, vol. 15, no. 6, pp. 313–318, 2015.

[5] K. Murawski, "New vision sensor to measure gas pressure," *Meas. Sci. Rev.*, vol. 15, no. 3, pp. 132–138, 2015.

[6] S. V. Ponomarev, "Stability analysis of a semiglobal algorithm for stereo vision in the soft-approach problem," *J. Opt. Technol.*, vol. 81, no. 11, pp. 651–655, 2014.

[7] M. T. El-Haddad and Y. K. Tao, "Automated stereo vision instrument tracking for intraoperative OCT guided anterior segment ophthalmic surgical maneuvers," *Biomed. Opt. Express*, vol. 6, no. 8, pp. 3014–3031, 2015.

[8] S. V. Murav'eva, O. A. Vakhrameeva, S. V. Pronin, and Y. E. Shelepin, "Comparing monocular and binocular visual acuity under noisy conditions," *J. Opt. Technol.*, vol. 82, no. 10, pp. 663–666, 2015.

[9] T. Nakazawa and A. Samara, "Three-dimensional inline inspection for substrate warpage and ball grid array coplanarity using stereo vision," *Appl. Opt.*, vol. 53, no. 14, pp. 3101–3109, 2014.

[10] P. Kiddee, Z. Fang, and M. Tan, "A practical and intuitive calibration technique for cross-line structured light," *Optik*, vol. 127, no. 20, pp. 9582–9602, 2016.

[11] G. Xu, X. Zhang, J. Su, X. Li, and A. Zheng, "Solution approach of a laser plane based on Plücker matrices of the projective lines on a flexible 2D target," *Appl. Opt.*, vol. 55, no. 10, pp. 2653–2656, 2016.

[12] P. Kiddee, Z. Fang, and M. Tan, "An automated weld seam tracking system for thick plate using cross mark structured light," *Int. J. Adv. Manuf. Technol.*, vol. 87, nos. 9–12, pp. 3589–3603, 2016.

[13] J.-E. Ha and K.-W. Her, "Calibration of structured light stripe system using plane with slits," *Opt. Eng.*, vol. 52, no. 1, p. 013602, 2013.

[14] G. Xu, Z. Hao, X. Li, J. Su, H. Liu, and L. Sun, "An optimization solution of a laser plane in vision measurement with the distance object between global origin and calibration points," *Sci. Rep.*, vol. 5, Jul. 2015, Art. no. 11928.

[15] M. Ritter, T. Dziomba, A. Kranzmann, and L. Koenders, "A landmark-based 3D calibration strategy for SPM," *Meas. Sci. Technol.*, vol. 18, no. 2, pp. 404–414, 2007.

[16] Y. I. Abdel-Aziz, H. M. Karara, and M. Hauck, "Direct linear transformation from comparator coordinates into object space coordinates in close-range photogrammetry," *Photogramm. Eng. Remote Sens.*, vol. 81, no. 2, pp. 103–107, 2015.

[17] J. A. M. Rodríguez, "Laser imaging and approximation networks for calibration of three-dimensional vision," *Opt. Laser Technol.*, vol. 43, no. 3, pp. 491–500, 2011.

[18] Z. Zhang, "A flexible new technique for camera calibration," *IEEE Trans. Pattern Anal. Mach. Intell.*, vol. 22, no. 11, pp. 1330–1334, Dec. 2000.

[19] G. Xu, A. Zheng, X. Li, and J. Su, "A method to calibrate a camera using perpendicularity of 2D lines in the target observations," *Sci. Rep.*, vol. 6, Oct. 2016, Art. no. 34951.

[20] Z. Zhang, "Camera calibration with one-dimensional objects," *IEEE Trans. Pattern Anal. Mach. Intell.*, vol. 26, no. 7, pp. 892–899, Jul. 2004.

[21] Y. Zhao and W. Li, "Self-calibration of a binocular vision system based on a one-dimensional target," *J. Mod. Opt.*, vol. 61, no. 18, pp. 1529–1537, 2014.

[22] A. Y. Poroikov, "Reconstruction of 3D profile of a deformed metallic plate by means of the image pattern correlation technique," *Meas. Techn.*, vol. 57, no. 4, pp. 390–395, 2014.

[23] A. Moeini and H. Moeini, "Pose-invariant gender classification based on 3D face reconstruction and synthesis from single 2D image," *Electron. Lett.*, vol. 51, no. 10, pp. 760–762, 2015.

[24] B.-K. Koo and J.-H. Kim, "Linear stratified approach using full geometric constraints for 3D scene reconstruction and camera calibration," *Opt. Express*, vol. 21, no. 4, pp. 4456–4474, 2013.

[25] G. Xu, J. Yuan, X. Li, and J. Su, "Reconstruction method adopting laser plane generated from RANSAC and three dimensional reference," *MAPAN*, pp. 1–13, Feb. 2018, doi: 10.1007/s12647-018-0252-x.

[26] G. Xu, J. Yuan, X. Li, and J. Su, "Profile reconstruction method adopting parameterized re-projection errors of laser lines generated from bi-cuboid references," *Opt. Express*, vol. 25, no. 24, pp. 29746–29760, 2017.

[27] G. Xu, J. Yuan, X. Li, and J. Su, "Optimization reconstruction method of object profile using flexible laser plane and bi-planar references," *Sci. Rep.*, vol. 8, Jan. 2018, Art. no. 1526.

[28] R. Hartley and A. Zisserman, *Multiple View Geometry in Computer Vision*. Cambridge, U.K.: Cambridge Univ. Press, 2003.

[29] R. A. Horn and C. R. Johnson, *Matrix Analysis*. Cambridge, U.K.: Cambridge Univ. Press, 2012.

[30] J. B. Ryu, C. G. Lee, and H. H. Park, "Formula for Harris corner detector," *Electron. Lett.*, vol. 47, no. 3, pp. 180–181, 2011.

GUAN XU was born in Changchun, Jilin, China, in 1981. He received the B.S., M.S., and Ph.D. degrees in vehicle operation engineering from Jilin University, Jilin, in 2003, 2006, and 2009, respectively. His research interests include active vision and binocular vision in vehicle inspection techniques.
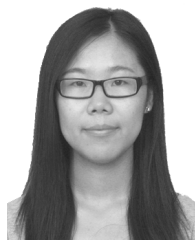
JING YUAN was born in Qiqihar, Heilongjiang, China, in 1992. She received the B.S. degree in vehicle operation engineering from Jilin University, Jilin, China, in 2016. Her research interests include active vision and 3-D reconstruction in vehicle inspection techniques.

XIAOTAO LI was born in Changchun, Jilin, China, in 1980. She received the B.S., M.S., and Ph.D. degrees in mechanical engineering from Jilin University, Jilin, in 2010. Her research interests include vision-based measurement and MEMS.

● ● ●